

## The Current Feedback on Stress Modifies the Ekman Buoyancy Flux at Fronts

JACOB O. WENEGRAT<sup>1</sup><sup>a</sup>

<sup>a</sup> Department of Atmospheric and Oceanic Science, University of Maryland, College Park, College Park, Maryland

(Manuscript received 13 January 2023, in final form 21 September 2023, accepted 22 September 2023)

**ABSTRACT:** Ocean surface currents introduce variations into the surface wind stress that can change the component of the stress aligned with the thermal wind shear at fronts. This modifies the Ekman buoyancy flux, such that the current feedback on the stress tends to generate an effective flux of buoyancy and potential vorticity to the mixed layer. Scaling arguments and idealized simulations resolving both mesoscale and submesoscale turbulence suggest that this pathway for air-sea interaction can be important both locally at individual submesoscale fronts with strong surface currents—where it can introduce equivalent advective heat fluxes exceeding several hundred watts per square meter—and in the spatial mean where it reduces the integrated Ekman buoyancy flux by approximately 50%. The accompanying source of surface potential vorticity injection suggests that at some fronts the current feedback modification of the Ekman buoyancy flux may be significant in terms of both submesoscale dynamics and boundary layer energetics, with an implied modification of symmetric instability growth rates and dissipation that scales similarly to the energy lost through the negative wind work generated by the current feedback. This provides an example of how the shift of dynamical regimes into the submesoscale may promote the importance of air-sea interaction mechanisms that differ from those most active at larger scale.

**KEYWORDS:** Atmosphere-ocean interaction; Eddies; Fronts; Ocean dynamics

### 1. Introduction

The mechanisms of air-sea interaction and coupling have been the subject of extensive study at scales of 10–100 km in the ocean mesoscale. Emerging from this work is a robust picture of the importance of air-sea interactions—where variability in ocean surface currents and sea surface temperature drive variability in the atmosphere which then can feedback on the ocean evolution through modifications to the surface fluxes of heat and momentum (Seo et al. 2023). Interactions of this type have been documented to be important across a wide range of processes in both the atmosphere and the ocean: from global climate variability such as El Niño (Pacanowski 1987; Luo et al. 2005), to basin-scale features such as the Gulf Stream path and stability (Renault et al. 2016a, 2019a), and down to the energetics of the ocean mesoscale eddy field, which holds the majority of the kinetic energy of the general circulation (Dewar and Flierl 1987; Ferrari and Wunsch 2009; Xu et al. 2016; Bishop et al. 2020; Rai et al. 2021).

At the same time, over the last several decades it has also become evident that the surface ocean is rich with variability at the submesoscale, which is best defined dynamically as flows with  $\mathcal{O}(1)$  Richardson and Rossby numbers (generally found at horizontal scales from 100 m to 10 km). Processes at these scales are critical to both local ocean boundary layer dynamics and biogeochemistry, and may play a significant role in regional, or global, integrated air-sea heat fluxes, seasonal energetics of the mesoscale, and pathways between the surface and interior (Su et al. 2018; Wenegrat et al. 2018; Schubert et al. 2020; Naveira Garabato et al. 2022; Taylor and Thompson 2023). Likewise, many features of larger-scale ocean variability, such as western boundary currents and mesoscale eddies, are now

recognized to have embedded sharp fronts and other features that fall in the submesoscale regime (Thomas et al. 2013; Brannigan et al. 2017; Zhang and Qiu 2018). However, despite the advances in understanding ocean circulation at the submesoscale, the role of submesoscale variability in air-sea interaction—and whether there are significant coupled interactions at this scale—remains less established.

Prior work using numerical modeling and observations suggest that some of the known physical pathways for air-sea interaction at the ocean mesoscale are also likely active at the submesoscale. This includes both thermal interactions, whereby variations in surface temperature induce changes in surface winds (Wenegrat and Arthur 2018; Shao et al. 2019; Sullivan et al. 2020), and the modulation of surface momentum fluxes by ocean surface currents. This last mechanism in particular has been identified as important in ocean simulations, where inclusion of the surface current feedback on the stress (CFB) introduces anticorrelations between surface stress anomalies and surface currents that act as a damping term in the kinetic energy equation (Duhaut and Straub 2006). This “eddy-killing” effect has been demonstrated to significantly modify the flux of kinetic energy between the mesoscale and submesoscale, and from the submesoscale ocean to the atmosphere (Renault et al. 2018). In this manuscript, however, the focus is on an alternate physical mechanism through which the CFB can also affect ocean dynamics and energetics at sharp fronts, through modifications of the cross-frontal advection of buoyancy—a key driver of submesoscale variability.

Winds blowing parallel to fronts generate a cross-front transport of buoyancy, termed the Ekman buoyancy flux (EBF; Thomas and Ferrari 2008). The strong buoyancy gradients at submesoscale fronts allow even moderate winds to generate extremely large magnitude EBF, with observed values exceeding the equivalent of an  $\mathcal{O}(10\,000)\text{ W m}^{-2}$  surface heat flux (D’Asaro et al. 2011; Thomas et al. 2013). This advective flux overwhelms surface heat fluxes between the atmosphere and

Corresponding author: Jacob O. Wenegrat, wenegrat@umd.edu

ocean, and hence is a central component of the mixed layer buoyancy budget at fronts (Johnson et al. 2020a,b). Further, the EBF helps set the rate of the frictional surface flux of potential vorticity (PV)—a dynamical tracer—with surface PV destruction leading to submesoscale frontogenesis, the emergence of fast-growing symmetric instabilities, and the generation of extremely strong boundary layer turbulence (Thomas and Lee 2005; D'Asaro et al. 2011; Thomas et al. 2013). The purpose of this manuscript is to document how the modulation of surface momentum fluxes by ocean surface currents also introduces modulations of the EBF at submesoscale fronts, leading to an effective source of buoyancy and PV to the ocean mixed layer which may alter the evolution of submesoscale fronts. This mechanism is likely to be significant primarily in cases of submesoscale fronts with strong surface currents, as are frequently seen within energetic larger-scale features such as western boundary currents and along the periphery of some mesoscale eddies.

The manuscript is structured as follows. In section 2 the basic theory of how the current feedback on stress modifies the surface Ekman buoyancy flux is introduced, along with scalings to determine its importance relative to the standard formulation of the EBF. In section 3 an idealized numerical model is introduced and used to validate several of the scalings and establish the quantitative effect. The potential importance of this mechanism relative to other processes active at the submesoscale is discussed in section 4, and results are summarized in section 5.

## 2. Current feedback on stress and the Ekman buoyancy flux

### a. Current feedback on stress

The origin of the CFB is evident through a simple kinematic consideration of the surface stress, which is a function of the wind speed *relative* to the surface ocean currents. When the surface current flows in the same direction as the wind, the relative wind speed (the difference in speed between the atmosphere and ocean) is reduced, reducing the surface stress. In contrast, when wind and currents are in opposing directions the relative wind speed is increased, and the surface stress is enhanced. The bulk surface stress incorporating this effect can be written as

$$\tau = \rho_a c_d |\mathbf{U}_a - \mathbf{u}_o| (\mathbf{U}_a - \mathbf{u}_o), \quad (1)$$

where  $\rho_a$  is the density of air,  $c_d$  is the surface drag coefficient,  $\mathbf{U}_a$  is the surface wind vector, and  $\mathbf{u}_o$  is the surface ocean current vector. From this a stress anomaly due to the CFB can be defined as

$$\tau' = \tau - \underbrace{\rho_a c_d |\mathbf{U}_a| \mathbf{U}_a}_{\bar{\tau}}, \quad (2)$$

where  $\bar{\tau}$  is the standard bulk stress defined using the Earth-relative wind vector. The total wind stress thus consists of a portion due solely to the winds, and an anomaly term due to the CFB.

It is also useful to develop approximate versions of (1) and (2) by noting that generally  $|\mathbf{u}_o| \ll |\mathbf{U}_a|$ , such that terms that are quadratic in the ocean surface velocity can be neglected

(Bye 1985; Rooth and Xie 1992; Duhaut and Straub 2006; Renault et al. 2017)

$$\tau \approx \rho_a C_d |\mathbf{U}_a| \mathbf{U}_a - 2\rho_a c_d |\mathbf{U}_a| \|\mathbf{u}_o\| \mathbf{e}, \quad (3)$$

where  $\mathbf{e} = \cos\theta \mathbf{i} + 0.5 \sin\theta \mathbf{j}$ , with  $(\mathbf{i}, \mathbf{j})$  defining an orthonormal basis where  $\mathbf{i}$  is aligned with the direction of the surface wind, and  $\theta$  is the angle between the surface wind and surface currents. Renault et al. (2017, their supplementary information) show that the angle between the surface current and  $\mathbf{e}$  cannot exceed  $19.5^\circ$ , such that  $|\mathbf{u}_o| \mathbf{e} \approx |\mathbf{e}| \mathbf{u}_o$ . It can further be assumed that—when considering mesoscale and submesoscale surface currents— $\theta$  has a uniform random distribution<sup>1</sup> such that the surface stress anomaly can be approximated as (Renault et al. 2017)

$$\tau' \approx -\frac{3}{2} \rho_a c_d |\mathbf{U}_a| \mathbf{u}_o. \quad (4)$$

In the following discussion  $\bar{\tau}$  is referred to as the background wind stress, and  $\tau'$  as the anomaly due to the CFB. Note, however, that while the approximate form of the stress, (4), is used in scaling arguments and for conceptual discussion, calculations involving the numerical model rely on the full surface stress (1), or stress anomaly (2), without approximation. Importantly, it can be clearly seen from (4) that the CFB-induced stress anomaly acts to oppose surface currents, such that it acts as a sink of kinetic energy through the surface wind work term—the eddy-killing effect of the CFB. It is shown below that this alignment of the stress anomaly with the surface currents also has dynamical and energetic consequences for submesoscale flows through the Ekman transport of buoyancy.

### b. Ekman buoyancy flux

At fronts, winds generate an advective flux of buoyancy, defined as (Thomas and Ferrari 2008)

$$\text{EBF} = \frac{\tau \times \hat{\mathbf{k}}}{\rho_o f} \cdot \nabla_h b, \quad (5)$$

where  $\rho_o$  is the density of seawater,  $b$  is the buoyancy, and  $\nabla_h$  is the horizontal gradient operator. This can also be directly related to the wind-driven component of the surface PV flux, which goes as  $J_{\text{WIND}} \approx f \text{EBF}/h$ , where  $h$  is the depth of the well-mixed portion of the surface boundary layer (Thomas and Ferrari 2008; Wenegat et al. 2018). When the winds are oriented in the “upfront” direction (opposing the surface thermal wind shear) the transport is toward the dense side of the front, acting as a buoyancy and PV source to the mixed layer. In contrast “downfront” winds in the direction of the surface thermal wind shear transport dense water over light, driving turbulent mixing and destroying PV.

Expanding the definition of the EBF using the wind stress given by (1) and (2) shows how the CFB can modify the surface EBF

<sup>1</sup> This assumption is taken only for conceptual simplicity and is not strictly necessary as  $|\mathbf{e}| = 1/2\sqrt{1 + 3 \cos(\theta)^2}$  such that it is always on the interval  $(0.5, 1)$  (Renault et al. 2017).

$$\text{EBF} = \underbrace{\frac{\bar{\tau} \times \hat{\mathbf{k}}}{\rho_o f} \cdot \nabla_h b}_{\text{EBF}_{\bar{\tau}}} + \underbrace{\frac{\boldsymbol{\tau}' \times \hat{\mathbf{k}}}{\rho_o f} \cdot \nabla_h b}_{\text{EBF}_{\boldsymbol{\tau}'}}. \quad (6)$$

The strength of the CFB effect on EBF can be estimated using (4),

$$\text{EBF}_{\boldsymbol{\tau}'} \approx -\left(\frac{3 \rho_a c_d}{2 \rho_o |f|}\right) |\mathbf{U}_a| |\mathbf{u}_o| |\nabla_h b| \cos \phi, \quad (7)$$

where  $\phi$  is the angle between the surface currents and the surface thermal wind shear.

Equation (7) indicates that the CFB may generate significant buoyancy—and PV—fluxes in the presence of strong surface currents aligned with sharp fronts. For illustration, posing this as an effective Ekman heat flux ( $\text{EHF} = \rho_o c_w \alpha^{-1} g^{-1} \text{EBF}$ , where  $c_w$  is the specific heat of seawater and  $\alpha$  is the thermal expansion coefficient) shows that the CFB can generate equivalent advective heat fluxes of  $\mathcal{O}(1000) \text{ W m}^{-2}$  at strong submesoscale fronts [using values observed in the Kuroshio by D'Asaro et al. (2011), where  $|\mathbf{U}_a| \sim 10 \text{ m s}^{-1}$ ,  $|\mathbf{u}_o| \sim 1 \text{ m s}^{-1}$ , and  $|\nabla_h b| \sim 10^{-5} \text{ s}^{-2}$ ]. Below it is argued that the frequent alignment of surface currents and surface thermal wind shear implies that the CFB will generally reduce the downfront component of the surface wind stress, acting to generate an effective source of buoyancy—and PV—to the mixed layer.

Finally, to further contextualize the importance of the CFB on EBF it is useful to compare the anomaly term to the standard formulation, which considers only the Earth-relative wind speed. The ratio of the two is given by

$$\frac{\text{EBF}_{\boldsymbol{\tau}'}}{\text{EBF}_{\bar{\tau}}} \sim -\frac{U_o}{U_a} \frac{\cos \phi}{\cos \psi}, \quad (8)$$

where  $U_o$  and  $U_a$  respectively scale the magnitude of the surface current and winds, and  $\psi$  is the angle between the wind and the surface thermal wind shear. This ratio also scales the relative importance of the CFB to background wind-driven PV fluxes. Notably, (8) does not depend directly on the strength of the buoyancy gradient, and instead depends only on the relative magnitudes of the surface current and wind speed, and their alignment with the front. Generally, the ratio of the velocity magnitudes will be small, although not always negligibly so in cases of weak or moderate winds and strong surface flows. However, despite this, the tendency of surface currents to align with fronts (i.e., for  $\phi$  to be small) allows the CFB contribution to play an important role in cases where winds and fronts are not aligned, or when integrating across many fronts where  $\text{EBF}_{\bar{\tau}}$  is of alternating sign (such that  $\int_A \cos \psi dA \approx 0$ ).

### 3. Results from numerical simulations

#### a. Description of simulations

Numerical simulations were performed using the Coastal and Regional Ocean Community (CROCO) model (Auclair et al. 2022). The domain was configured as an idealized reentrant channel, with 500-km length in the periodic  $x$  direction, 2000 km

in the  $y$  direction (bounded by free-slip walls), and a uniform depth of 4000 m. The vertical direction was discretized with 100 stretched vertical levels, with near-surface resolution of  $\Delta z = 3.6$  m, and the  $K$ -profile parameterization was used for the turbulence closure (KPP; Large et al. 1994). Existing turbulence closures are known to not accurately represent all pathways for the generation of turbulence at fronts (Bachman et al. 2017; Chor et al. 2022); however, exploration of the sensitivity of results to the choice of turbulence closures is beyond the scope of the present work.

The flow was initialized in geostrophic balance, with a baroclinically unstable horizontal buoyancy gradient [a detailed description of the initial frontal configuration can be found in Soufflet et al. (2016)]. An alternate configuration with an imposed initial mixed layer was tested and found to not qualitatively alter the results. The simulation was first allowed to evolve with no surface forcing for 360 days at mesoscale resolving resolution ( $\Delta x = \Delta y = 2$  km), during which time the temperature front was maintained by relaxation toward the initial condition. At the end of the 360-day spinup period there is an active field of mesoscale eddies, and the eddy kinetic energy has reached a quasi-steady state. The simulation was then restarted at submesoscale permitting resolution ( $\Delta x = \Delta y = 500$  m), without relaxation, allowing the rapid growth of submesoscale mixed layer instabilities, characterized by  $\mathcal{O}(1)$  Rossby numbers (Fig. 1). It is computationally prohibitive to run a domain of this size at sufficient resolution to directly resolve symmetric instabilities (SI), hence some of the discussion around the potential impacts of the CFB on boundary layer energetics are posed as hypotheses in section 4.

The high-resolution simulation was forced by a uniform surface heat loss of  $25 \text{ W m}^{-2}$  (unless otherwise noted) and a moderate surface wind of  $|\mathbf{U}_a| = 7 \text{ m s}^{-1}$  oriented toward the northeast direction. The surface stress was calculated using (1) with a constant drag coefficient of  $c_d = 10^{-3}$ . This simplified calculation of the surface stress isolates only the direct effect of the surface currents on the wind stress, and does not include other air-sea interaction mechanisms such as thermal feedbacks on the wind or drag coefficient, or the response of the winds to the CFB modifications in stress. This last mechanism in particular will tend to counter the CFB, as the reduction of surface stress due to the CFB can generate a partially compensating increase in surface winds (Renault et al. 2016b). This effect can be parameterized in uncoupled models by writing the relative wind vector as  $\mathbf{U}_a - (1 - s_w)\mathbf{u}_o$  such that  $s_w > 0$  accounts for the increase of the wind speed due to the CFB (Renault et al. 2016b). Noting that the perturbation stress is approximately linear in the surface current it follows that the magnitude of  $\text{EBF}_{\boldsymbol{\tau}'}$  would also be reduced by a factor of approximately  $(1 - s_w)$  (as would other CFB effects such as the modification of the surface wind work). Estimates from a coupled global mesoscale resolving simulation suggest  $s_w = 0 - 0.5$ , with a global mean value of  $s_w \approx 0.3$  (Renault et al. 2019b). However, it is not currently clear whether this value is representative of this effect at the submesoscale—where the small horizontal length scales limit the ability of the atmospheric boundary layer to respond locally (Wenegrat and Arthur 2018)—and so this effect is not directly estimated here.

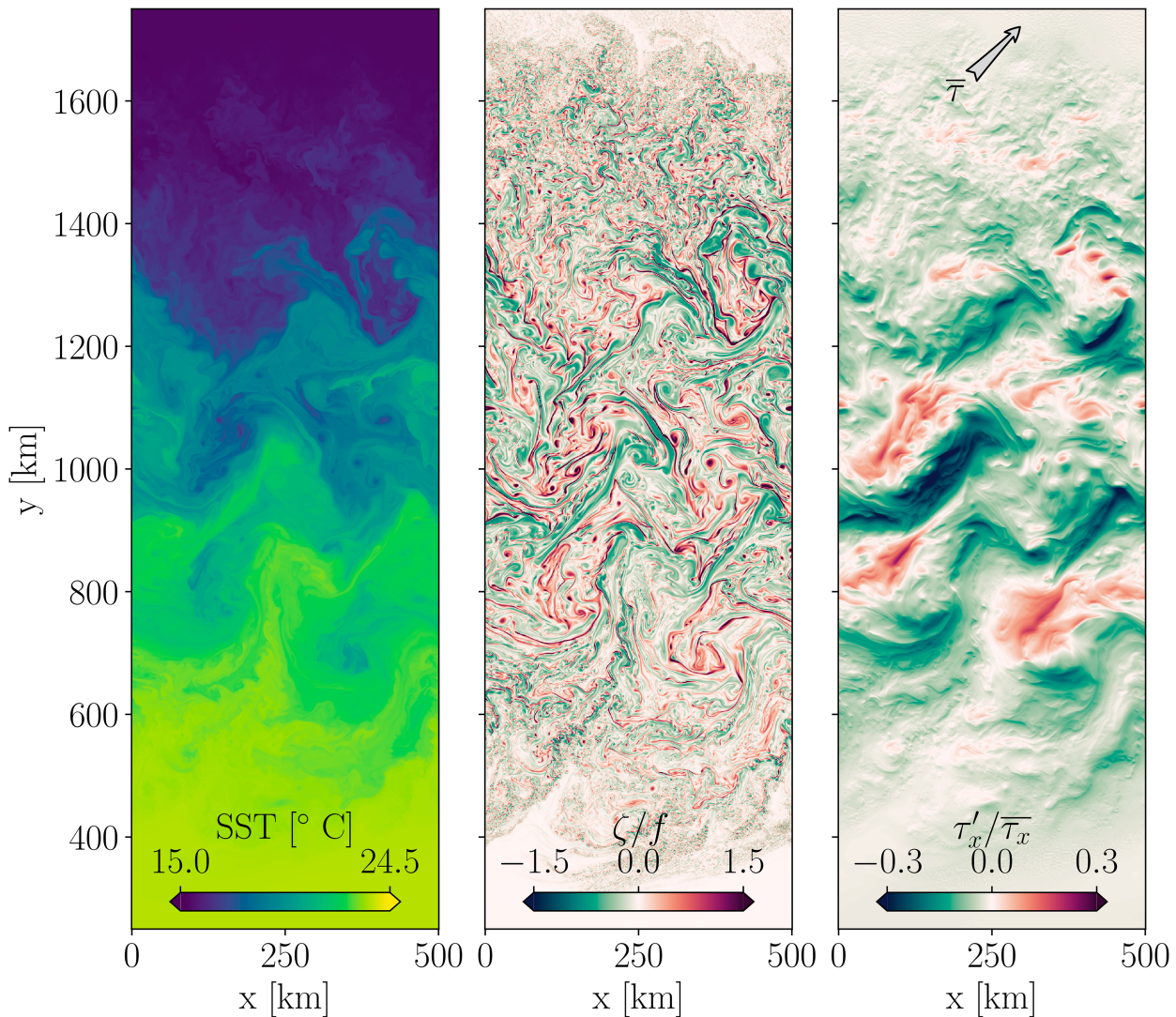


FIG. 1. (left) Sea surface temperature, (center) surface relative vorticity normalized by the Coriolis frequency, and (right) the zonal component of the wind stress anomaly introduced by the current feedback normalized by the standard Earth-relative formulation of the zonal wind stress. The ocean surface velocity field imprints on the surface wind stress via the CFB mechanism, introducing correlations between surface currents, horizontal buoyancy gradients, and wind stress. The background wind stress direction is indicated by the gray arrow. All fields are shown on day 385 (25 days after restart).

A high-resolution control simulation was also performed without the CFB (referred to as run “No-CFB” throughout), such that the total wind stress is given by  $\bar{\tau}$  in Eq. (2).

Before discussing the EBF it is useful to first note several differences between the simulation with the CFB and the No-CFB control simulation without, although it is not implied these changes are solely attributable to changes in the EBF. Both simulations have kinetic energy spectral slope shallower than  $k^{-3}$  through the submesoscale (Fig. 2), consistent with realistic models and observations (Capet et al. 2008; Callies et al. 2015; Qiu et al. 2017; Soares et al. 2022). The amount of kinetic energy in the submesoscale is, however, reduced by approximately 15% in the CFB simulation. This tendency of the CFB to weaken the submesoscale is also reflected in the vorticity, divergence, and

strain distributions (Fig. 3), which in each case show shifts toward zero in the distributions for the simulation run with the CFB. The surface vorticity in the CFB run shows considerably less negative values of vertical vorticity. Many of these features are also consistent with prior realistic simulations with the CFB; however, an advantage of the idealized setup used here is that because both the CFB and No-CFB simulations are started from a common spinup run—and only run for 30 days of simulation time—the mesoscale and larger flow remains relatively constant between the two runs with changes primarily in the emerging small scales. This acts to isolate changes at the submesoscale, in contrast to longer integrations where changes to the larger-scale circulation can generate indirect changes to the small-scale flow, in addition to the direct effects of the CFB (Renault et al. 2018).

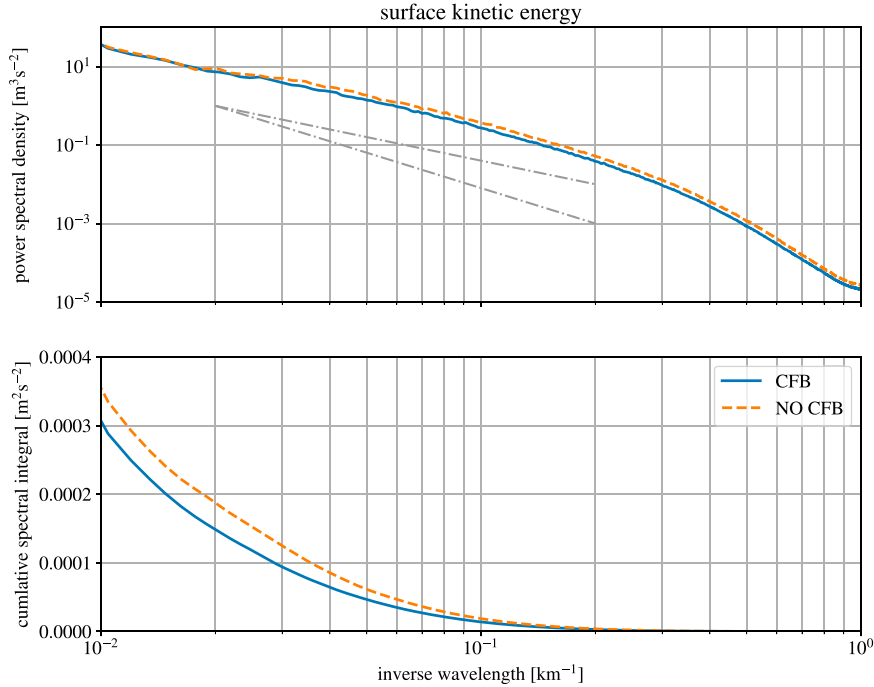


FIG. 2. (top) Isotropic power spectral density of the surface kinetic energy averaged over days 380–390, comparing the run with the current feedback on stress (CFB) to the run without (No-CFB). Example  $k^{-2}$  and  $k^{-3}$  spectral slopes are indicated by the dash-dot lines. (bottom) The cumulative spectral integral (integrated from high to low wavenumber).

### b. Validation of approximate forms

The numerical model is used to validate two of the approximations given in section 2, as shown in Fig. 4. First is the approximate form of  $\tau'$ , given in Eq. (4), which is compared to the exact calculation formed by subtracting  $\bar{\tau}$  from the full

surface stress, e.g., (2). Variance around the 1–1 line is generally small, and reflects the joint contributions of the assumptions that terms that are quadratic in the surface current are small, alignment of  $\mathbf{e}$  and  $\mathbf{u}_o$ , and that the angle of surface currents relative to the wind has a uniform random distribution.

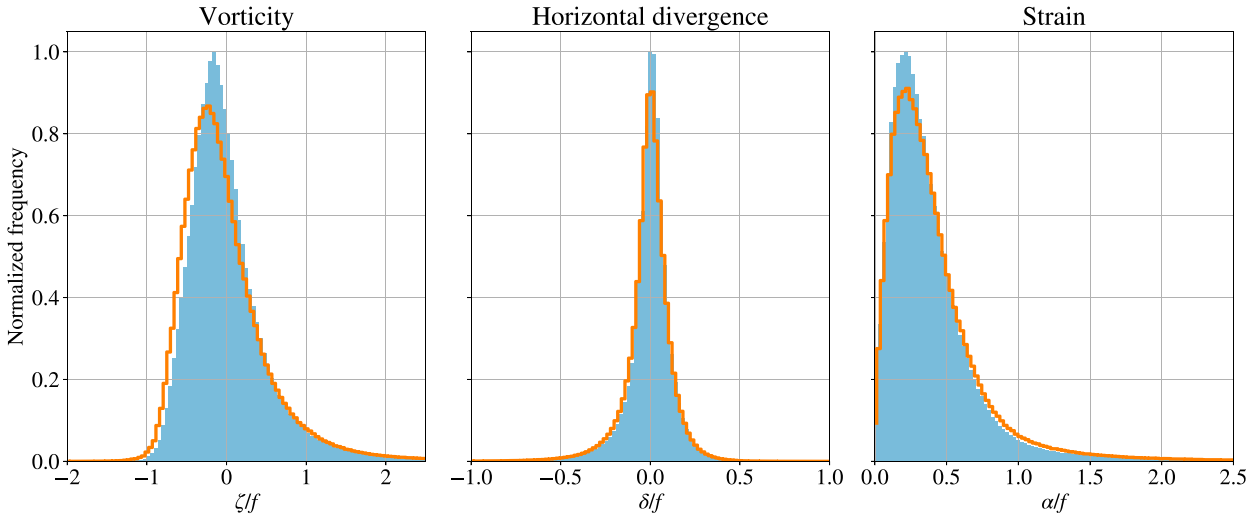


FIG. 3. (left) Histograms of the surface vertical vorticity, (center) surface horizontal divergence, and (right) surface strain comparing the simulation with the current feedback (CFB, blue) to the simulation run using only the Earth-relative surface wind stress (No-CFB, orange). In each plot the distributions are normalized by the peak value in the distribution of simulation CFB, the  $x$  axis is normalized by the Coriolis frequency, and data covers the last 5 days of simulation time.

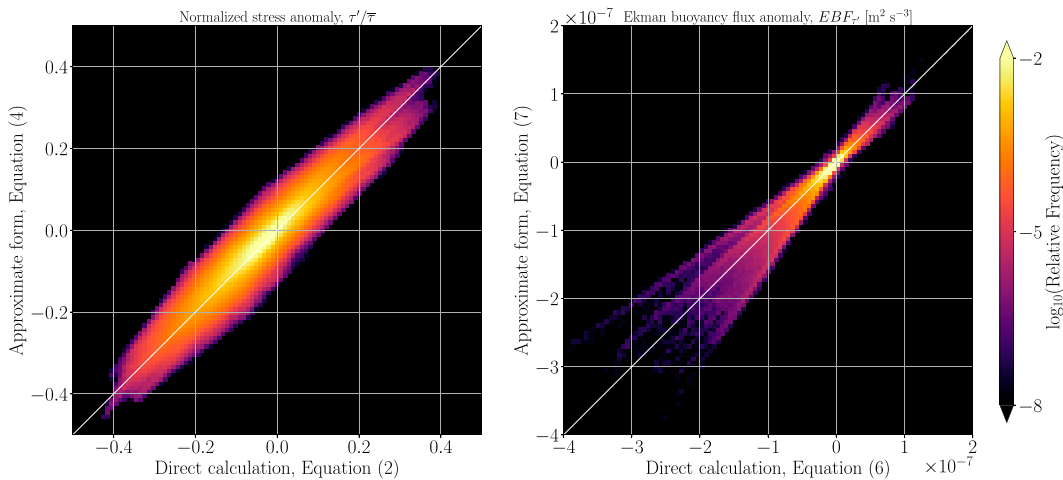


FIG. 4. Comparison of numerical results with approximate forms from section 2. (left) CFB induced stress anomaly, normalized by the standard bulk stress calculated using Earth-relative wind speeds. Both zonal and meridional components are included. (right) CFB induced Ekman buoyancy flux anomaly. In both panels the color scale shows the relative frequency of occurrence over simulation days 365–390 (normalized such that the sum of all bins is one), and the 1–1 line is indicated in white.

Equation (4) thus provides a useful scaling of the strength of the CFB effect on the surface stress. The approximate form of the  $EBF_\tau$ , given by (7) likewise is able to reasonably approximate the true values, a result that follows from it adding no additional assumptions beyond the approximate form of the stress. Errors in the approximate form increase at extreme values of  $EBF_\tau$ , likely due to these values being controlled by just a few individual fronts such that the assumption used in deriving (4) of a uniform random distribution between surface currents and wind direction does not hold. The tendency of  $EBF_\tau$  to be negative (oriented downward such that it is a source in the mixed layer budget) is also evident and is discussed further below.

#### c. Changes to the Ekman buoyancy flux

A snapshot of the Ekman buoyancy flux is shown in Fig. 5, with units given as an equivalent heat flux for illustrative purposes. Values in this simulation reach extremes of  $\mathcal{O}(\pm 1000) \text{ W m}^{-2}$ , again emphasizing how at fronts these terms can exceed typical air-sea buoyancy fluxes. The scaling for the CFB-induced EBF relative to the background EBF, (8), highlights two particular frontal configurations where  $EBF_\tau$  may be significant locally at fronts. The first is the case of winds and fronts that are not aligned, as highlighted in the top row of Fig. 5. Here the winds are blowing in a direction aligned with the surface buoyancy gradient (across-front winds), but the CFB effect contributes as much as  $360 \text{ W m}^{-2}$  of effective downward heat flux into the mixed layer through the cross-frontal Ekman transport of buoyancy. This will act to restratify the front, and hence may suppress frontogenesis and the development of submesoscale instabilities through the associated surface PV injection. The other frontal configuration where scalings suggest significant contributions from  $EBF_\tau$  is the case of strong surface velocities, as shown in the bottom row of Fig. 5. Here the strong flow due to the large-scale

meandering of the jet leads to large surface velocities ( $\sim 1 \text{ m s}^{-1}$ ) that significantly reduce the stress. This acts as an effective source of downward EBF to the mixed layer, reducing the EBF due to downfront winds by approximately 25% (an effective change in the equivalent Ekman heat flux of approximately  $200 \text{ W m}^{-2}$ ). For this front the net EBF remains positive, representing a loss of buoyancy and PV at the surface; however, as boundary layer properties such as the turbulent dissipation generated by symmetric instability are sensitive to the magnitude of this flux (Taylor and Ferrari 2010), the CFB contribution may be significant to the net rate of energy extracted from the geostrophic flow by downfront winds (section 4).

The distribution of all values of  $EBF_\tau$  is shown in Fig. 6. Values range from approximately  $-1000$  to  $250 \text{ W m}^{-2}$ , with a peak around 0 that reflects the spatial intermittency of fronts. The largest values are associated with those regions with both strong fronts and strong surface currents, where from (8) the stress anomaly term can contribute significantly to the total EBF (note many regions where  $|\tau'_x/\tau_x| \geq 0.3$  in Fig. 1). The distribution of  $EBF_\tau$  is negatively skewed (a pattern which is also evident in the predominantly negative values in the right columns of Figs. 4 and 5). From (7) the sign of the perturbation EBF is set by the relative orientation of surface currents and fronts, with negative values resulting from surface currents that are in the direction of the thermal wind shear ( $|\phi| < \pi/2$ ). The joint distribution of thermal wind shear and surface current directions is plotted in Fig. 6, indicating that they are largely parallel.

To what extent is this a general feature in the ocean? A heuristic argument can be made by noting that many ocean fronts result from frontogenesis by the surface strain field, leading to alignment of fronts and streamlines, and that these fronts in turn act to help set the direction of the surface flow through their thermal wind shear (Eliot and Wenegrat 2021). Indeed the general principle of the alignment of fronts and surface flows

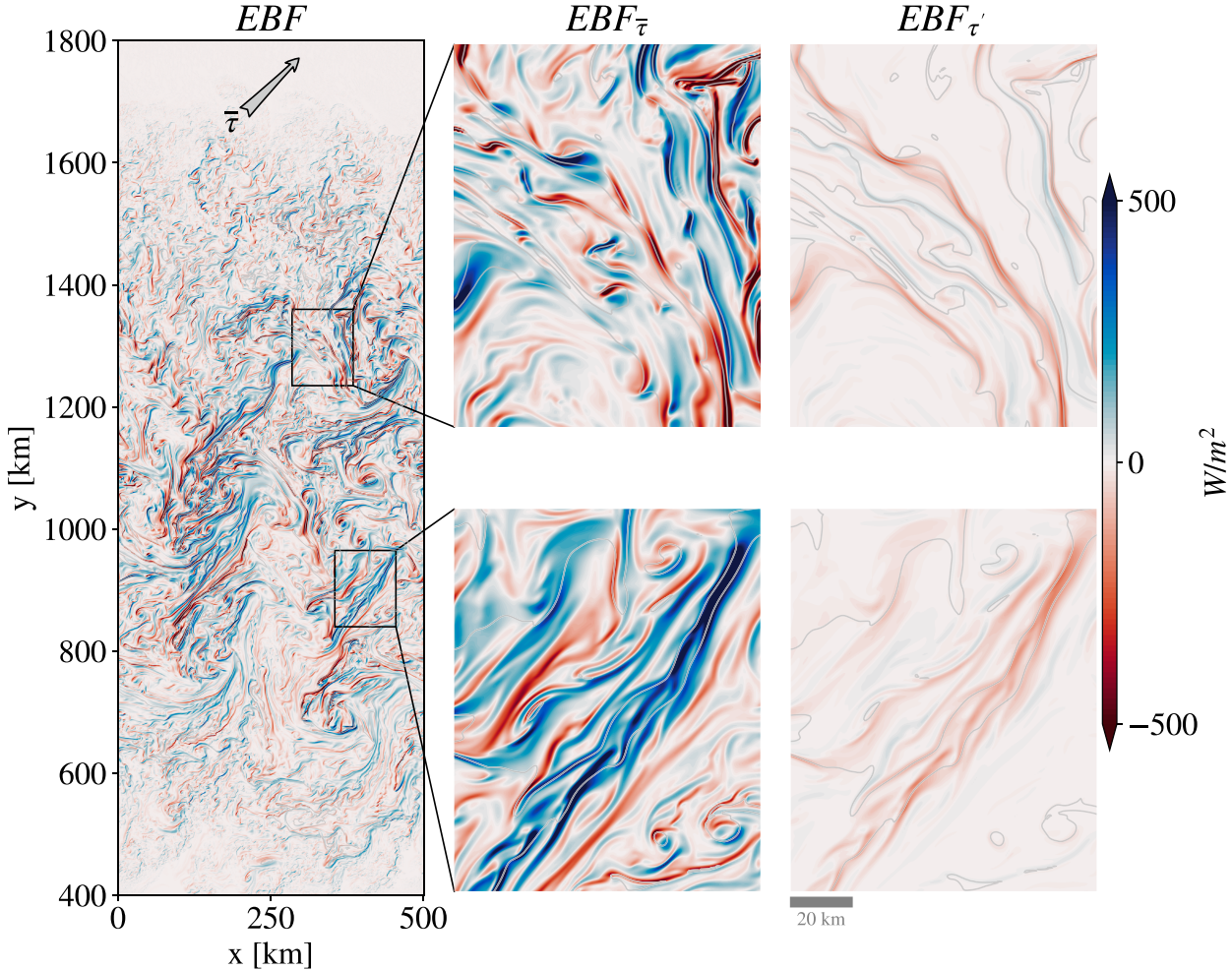


FIG. 5. (left) The Ekman buoyancy flux from the numerical model on day 385 (25 days after restart), along with (center) two zoomed-in regions of the background  $\overline{EBF}$  and (right) the current feedback on stress induced anomaly  $EBF_{\tau'}$ . The color scale is normalized to units of equivalent surface heat flux for illustrative purposes. Contours of surface temperature (thin gray lines), with  $1^{\circ}\text{C}$  intervals, are also shown to indicate frontal orientation (see also Fig. 1). The zoom regions are  $100 \text{ km} \times 125 \text{ km}$  in the  $x$  and  $y$  directions, respectively, and a scale bar is shown.

underpins some operational surface current retrieval algorithms (Isern-Fontanet et al. 2017). A more formal connection can be made via the relationship between the surface buoyancy and the geostrophic streamfunction in quasigeostrophic dynamics, where in the specific case of surface quasigeostrophic (SQG) flows the surface buoyancy defines the streamfunction such that fronts and surface currents are identically aligned (Lapeyre 2017). Variants of the SQG model show skill at reproducing surface currents in models and observations (Klein et al. 2008; González-Haro and Isern-Fontanet 2014; González-Haro et al. 2020; Miracca-Lage et al. 2022), although observed kinetic energy spectra are generally inconsistent with SQG predictions (Callies and Ferrari 2013; Chereskin et al. 2019; Soares et al. 2022). In more dynamically complex settings, for instance layered quasigeostrophic models that approximate the presence of a surface mixed layer, the total surface flow is a horizontal-scale-dependent function of buoyancy anomalies at multiple levels (Callies et al. 2016).

These results suggest an interpretation of  $EBF_{\tau'}$  as primarily acting as a source term (in buoyancy and PV) to the mixed layer, and it is straightforward to further simplify both (7) and (8) using an assumption of  $\phi = 0$ . However, it can also be seen that there are some regions where the surface flow opposes the surface thermal wind shear ( $\phi \approx \pm\pi$ ), flipping the sign of  $EBF_{\tau'}$  (Figs. 5 and 6). These cases tend to occur in this simulation as a result of the strong eastward jet, which when superimposed on weaker baroclinic shear flows can cause the total surface velocity (jet plus eddy contributions) to oppose the thermal wind shear in some places. These instances are associated both with weaker fronts (where the thermal wind contribution to the flow is smaller), and with smaller velocities as the jet and thermal wind flows oppose each other in the total surface current. These factors both act to lower the magnitude of  $EBF_{\tau'}$  (Fig. 6), limiting the impact of these events (cf. for instance regions of positive versus negative  $EBF_{\tau'}$  in Fig. 5), such that the occurrences of positive  $EBF_{\tau'}$  contribute only

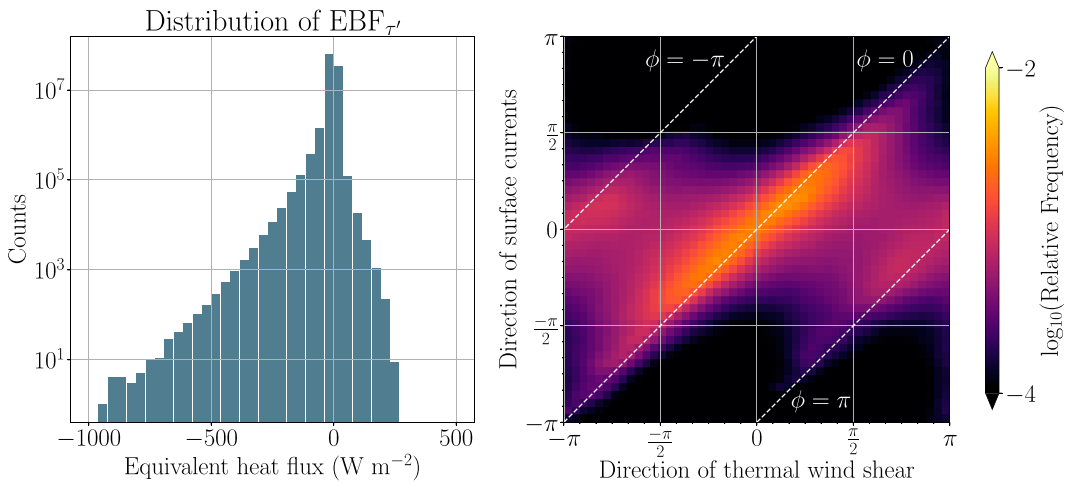


FIG. 6. (left) Distribution of the perturbation Ekman buoyancy flux,  $\text{EBF}_{\tau'}$ , with units given as an equivalent heat flux. (right) Joint distribution of the surface thermal wind shear direction (front direction) and the angle of the total surface currents. Angles are defined using the standard trigonometric convention. Cases of surface currents aligned with the surface thermal wind shear ( $\phi = 0$ ), and opposing the surface thermal wind shear ( $\phi = \pm\pi$ ), are indicated by the dashed white lines.

about 20% to the total sum. As such, the remainder of this manuscript focuses largely on the case where  $\phi \approx 0$  such that  $\text{EBF}_{\tau'} < 0$ .

The covariability between surface currents and fronts (e.g., Fig. 6) suggests that even weak surface currents may have area-integrated effects through the CFB. The best studied example of this is the so-called eddy-killing effect, which can be seen in Fig. 7 which provides a zoomed in view of a single cyclonic eddy. The CFB induces stress anomalies that are anticorrelated with the surface currents, creating negative wind-work that drains eddy kinetic energy. However, it can also be seen that in this case the cold-core eddy is associated with a buoyancy gradient that is positively correlated with the stress anomaly (shown in Fig. 7 in terms of the meridional gradient relevant to the zonal stress anomaly, although both zonal and meridional components show a similar pattern). This pattern of covariability between  $\tau'$  and  $\nabla_h b$  indicates that  $\text{EBF}_{\tau'} < 0$  when integrated across an eddy, in this case equivalent to an approximately  $-10 \text{ W m}^{-2}$  surface heat flux. The mean  $\text{EBF}_{\bar{\tau}'}$  over the eddy is about an order of magnitude smaller.

Integrating over larger areas likewise indicates a significant reduction of the total EBF by  $\text{EBF}_{\tau'}$  (Fig. 8). Over the whole frontal zone the total EBF is equivalent to an effective surface heat flux of  $5\text{--}10 \text{ W m}^{-2}$ , acting to cool the surface mixed layer, although these specific values are a function of the imposed mean wind and large-scale buoyancy gradient and hence cannot be generalized from these idealized simulations. More important is, however, the reduction of the area-integrated EBF by approximately 50% due to the CFB—a result that is predicted by (8) and the observed tendency for surface currents to be aligned with fronts. Similar results hold both within the center of the jet, where the flow is dominated by strong mesoscale features with large surface currents, and on the jet flanks where the fronts and flow are weaker and more isotropic (Fig. 8). In both cases the CFB reduces

the area-integrated EBF, although this effect is less pronounced in the weaker-front region, consistent with the dependence of (8) on the strength of the surface currents. That these changes between the CFB and No-CFB runs in each case are due to  $\text{EBF}_{\tau'}$  was confirmed by calculation of the integrated  $\text{EBF}_{\bar{\tau}'}$  from the CFB simulation, which also closely follows the No-CFB simulation (not shown), indicating there are not significant changes to the larger-scale mean horizontal buoyancy gradients between these runs.

#### d. Changes to the potential vorticity

Finally, beyond the mixed layer buoyancy budget, the EBF also affects the surface flux of Ertel PV, which exerts strong dynamical controls on ocean circulation, both locally in the boundary layer (Taylor and Ferrari 2010), and on the large-scale circulation as water masses are subducted into the interior (Marshall et al. 2001; Wenegrat et al. 2018). The connection between the EBF and surface PV flux at individual fronts is well established (Thomas and Ferrari 2008), and is thus not reiterated here other than to note that the changes in EBF by  $\text{EBF}_{\tau'}$  shown in Fig. 5 can also be interpreted directly in terms of a reduction of PV destruction by the EBF [see also Chen et al. (2022), who found a reduction in PV destruction in a simulation of a single submesoscale eddy that may be explained by the mechanism discussed here]. Here it is noted that the cumulative effect of this reduction appears in the volume-integrated PV budget of these simulations (Fig. 9). In both the CFB and No-CFB cases PV is destroyed, largely due to the imposed surface heat loss which is approximately 5 times larger for this simulation configuration than the mean Ekman heat flux (Fig. 8). However, the rate of PV destruction is reduced by approximately 15% when the CFB is included (this value includes the effect of the surface heat flux in the denominator). The CFB thus acts as an effective source of PV in these simulations (Fig. 9, bottom panel).

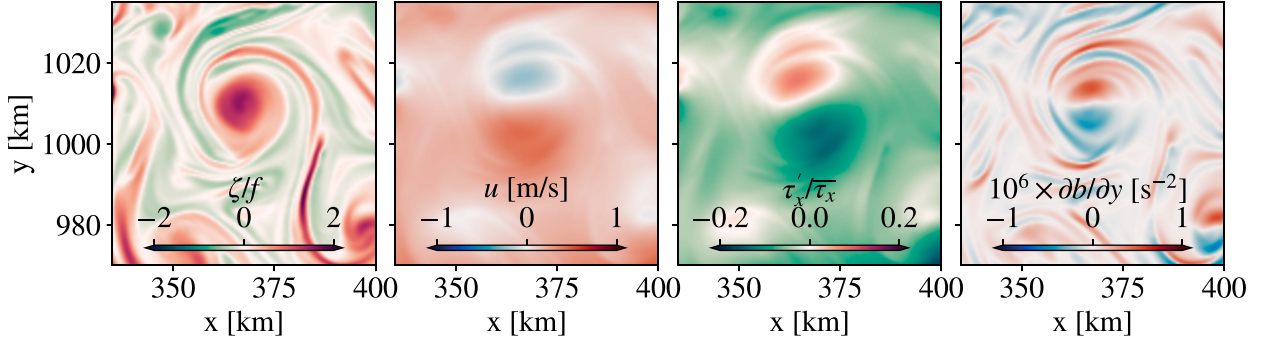


FIG. 7. Zoomed in region highlighting a single submesoscale cyclonic eddy in terms of (from left to right) surface relative vorticity normalized by the Coriolis frequency, zonal surface current, zonal component of the stress anomaly, and the meridional buoyancy gradient. Anticorrelations between surface currents and wind stress anomalies give rise to negative wind work (eddy-killing effect), whereas correlations between stress anomalies and buoyancy gradients are associated with a negative Ekman buoyancy flux that acts as a source of buoyancy in the mixed layer budget.

Simulations run with no surface buoyancy flux (CFB and No-CFB) are also shown for comparison (Fig. 9, dashed lines). The net evolution of the PV in this case is different, as expected without the strong (relative to the mean EBF) surface buoyancy loss acting to destroy PV. Notably without a surface buoyancy loss there is a net injection of PV in the case with the CFB, whereas the No-CFB case has a near-zero change over the simulation period. However, despite the differences in PV evolution, the change in the PV between CFB and No-CFB

cases is very similar across the configurations with and without surface buoyancy fluxes (Fig. 9, bottom panel). This effective PV injection by the CFB is consistent in sign and magnitude with the mean PV flux implied by  $\text{EBF}_{\tau'}$ , which can be very roughly estimated as  $J_{\text{EBF}_{\tau'}} \sim f \text{EBF}_{\tau'} / h$  such that the change in volume-averaged PV over the 30-day simulation period goes as  $\Delta q_{\text{EBF}'} \sim -J_{\text{EBF}_{\tau'}} \Delta t / \Delta z \approx 2.7 \times 10^{-11} \text{ s}^{-3}$  (using  $\text{EBF}_{\tau'}$  equivalent to a  $-5 \text{ W m}^{-2}$  heat flux, an average mixed layer depth of 45 m in the frontal zone, and a  $\Delta t$  of 30 days and  $\Delta z$  of 500 m for

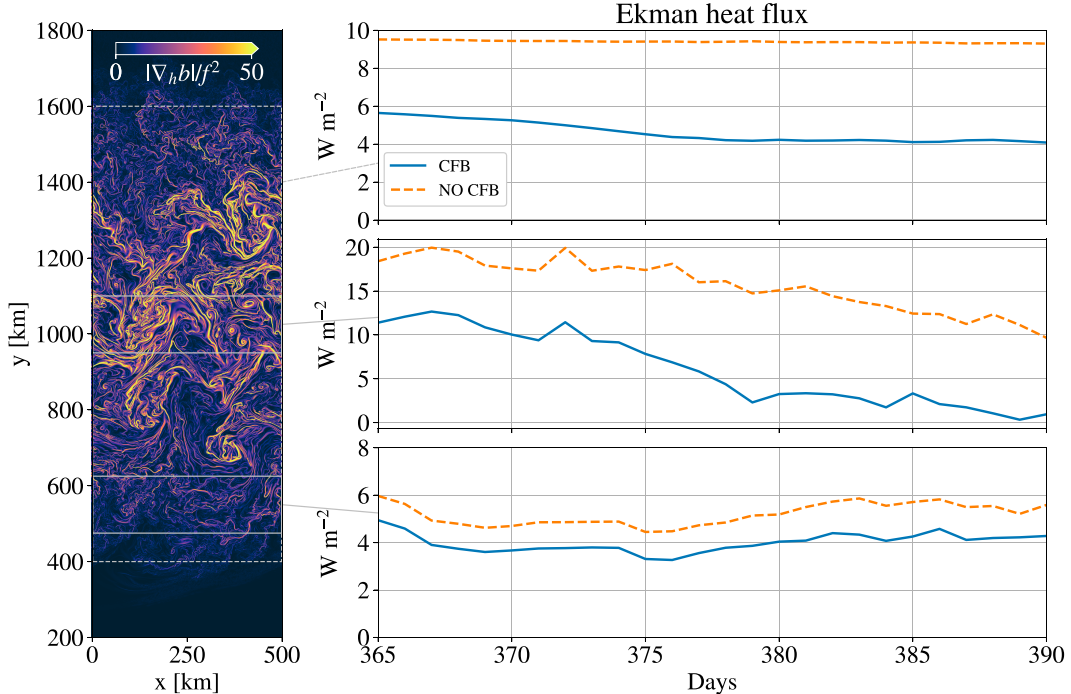


FIG. 8. (left) Magnitude of the surface horizontal buoyancy gradient on day 385 (25 days after restart), (right) along with (top) the spatial mean Ekman heat flux over the full frontal region (for  $y = [400, 1600 \text{ km}]$ ), (middle) a region of strong fronts (for  $y = [950, 1100 \text{ km}]$ ), and (bottom) a region of weaker fronts (for  $y = [475, 625 \text{ km}]$ ). The simulation run with the current feedback (CFB, solid blue line) can be compared to a simulation run with the standard Earth-relative formulation of the surface stress (NO-CFB, orange dashed line).

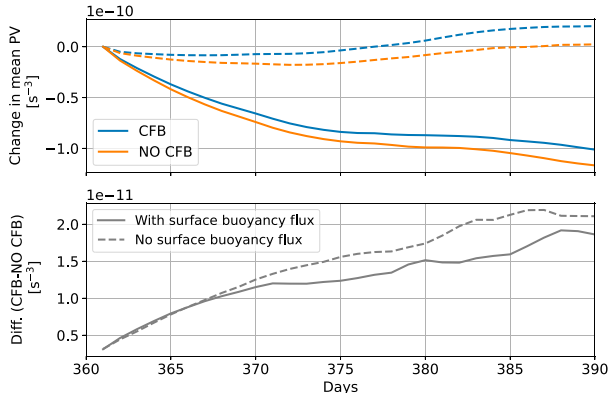


FIG. 9. Comparison of the change in Ertel PV volume-averaged between the surface and 500-m depth and  $y = 500\text{--}1500\text{ km}$  relative to day 361  $[V^{-1} \int_V q(t) - q(t_0) dV]$ . (top) The change in mean PV relative to the PV on day 361 immediately following the simulation restart for the CFB run (solid blue) and the No-CFB run (solid orange). (bottom) The difference in between the runs with and without the CFB. Results of a simulation run with no surface buoyancy flux are also shown (dashed lines in each subplot) for comparison.

comparison with the cumulative change in Fig. 9, bottom panel). This estimate is similar to the actual volume-integrated PV change due to the CFB in both simulations; however, a more complete attribution to  $\text{EBF}_r$  would require disentangling several mechanisms, and hence is beyond the scope of the present work (see discussion in section 4). Regardless, the changes in EBF and PV documented here suggest the CFB may be important in the PV budget both locally at fronts with strong surface currents or in cases of cross-frontal winds, and when considering the integrated contributions over many submesoscale fronts.

#### 4. Discussion

The idealized simulations considered here are designed to provide a simple illustration of the direct effect of the CFB on the EBF. However, they are also associated with a number of limitations—specifically in resolution and realism—that do not allow quantification of a number of additional aspects of how the CFB effect on EBF may be important for submesoscale dynamics and energetics. Several of these other mechanisms, and challenges for disentangling their effects, are discussed here.

Perhaps the most important limitation of the simulations considered in this manuscript is that they are not sufficiently high-resolution to permit symmetric instabilities, such that the direct energetic effects of  $\text{EBF}_r$  in the simulations cannot be usefully quantified. However, the reduction in surface EBF by the CFB is expected to affect symmetric modes in two ways. First, as shown above, the  $\text{EBF}_r$  acts primarily as a source term in the PV budget, which will tend to suppress the emergence of symmetric instabilities, potentially reducing the frequency of their occurrence. The net effect of this will vary depending on the forcing and how close to marginally stable to SI the fronts are, and cannot be estimated a priori. Second,

in the case of fronts where the net EBF remains positive (i.e., wind-driven PV destruction), the CFB will modify the magnitude of the energy extracted from the balanced flow through the geostrophic shear production (GSP) which scales with the EBF (Taylor and Ferrari 2010; Thomas et al. 2013). This energy is ultimately cascaded forward to turbulence (Chor et al. 2022), and hence the CFB is expected to act to reduce the SI-enhancement of turbulent dissipation by an amount

$$\overline{\text{GSP}} \approx \text{EBF}_r \frac{h}{2} \approx -\frac{3}{4} \frac{\rho_a}{\rho_o} c_d |\mathbf{U}_a| \|\mathbf{u}_o\| |\Delta \mathbf{u}_g|, \quad (9)$$

where the overline indicates a vertical integral over the mixed layer of depth  $h$ ,  $|\Delta \mathbf{u}_g| = h |\nabla_h b/f|$  is the magnitude of the change in geostrophic velocity over the mixed layer and it is assumed  $\phi = 0$ . For the observations of symmetric instability along the Kuroshio discussed in section 2 (D'Asaro et al. 2011), the strong surface currents ( $|\mathbf{u}_o| \approx 1.5 \text{ m s}^{-1}$ ) and modest winds ( $|\mathbf{U}_a| \approx 10 \text{ m s}^{-1}$ ) imply that  $\text{EBF}_r$  could reduce the vertically integrated turbulent dissipation rate by  $\mathcal{O}(10^{-5}) \text{ W m kg}^{-1}$ , about 15% of the total.

The CFB modification of the EBF may therefore act to reduce the rate of energy flux from the balanced flow to the submesoscale and dissipation, both through PV injection—which will reduce the frequency of symmetric instability—and through a direct modification of the growth rates via the change in EBF. This reduction of shear production and dissipation by SI can be compared to the loss of energy through the CFB wind-work anomaly, which goes as  $\rho_o^{-1} \tau' \cdot \mathbf{u}_o \approx -(3/2) \rho_o^{-1} \rho_a c_d |\mathbf{U}_a| |\mathbf{u}_o|^2$ . It is therefore anticipated that even in SI unstable conditions, the CFB will slow the instability growth rate through both a reduction in the GSP and the generation of negative wind-work, with relative contributions dependent on the ratio of  $|\Delta \mathbf{u}_g|/|\mathbf{u}_o|$ .

Aside from the limitations of resolution, it is also worth highlighting the challenge—even in these relatively simple numerical experiments—of definitively partitioning the observed changes in the submesoscale (see for instance Figs. 2 and 3) across the various processes affected by the CFB. An illustrative example of this challenge comes from considering the change in PV between the CFB and No-CFB runs (Fig. 9), which will be affected both by the  $\text{EBF}_r$ , and by changes to the strength of the turbulent thermal wind (TTW) secondary circulations driven by the mixing of geostrophic momentum at fronts (Wenegrat and McPhaden 2016; McWilliams 2017). The PV fluxes associated with the TTW flow depends on  $|\nabla_h b|^2$  (Wenegrat et al. 2018), and therefore may be sensitive to changes in the strength of submesoscale fronts introduced by the CFB, including changes forced directly by the  $\text{EBF}_r$  as well as those resulting from the reduction of mesoscale and submesoscale eddy kinetic energy by the surface wind work. Direct diagnosis of the relative contributions of changes in the EBF and TTW PV flux are confounded by both appearing in the PV budget via the same frictional flux terms, such that disentangling the mechanisms may require the design of more sophisticated numerical experiments than simple comparisons of runs with and without the CFB.

Finally, despite this challenge it is, however, worth noting that the simulations used here show a very slight reduction of

the magnitude of the horizontal buoyancy gradients in the CFB run (approximately 5%). This implies a reduction of TTW PV injection in the CFB case that is inconsistent with the observed increase in PV of the simulations with the CFB relative to No-CFB (Fig. 9), whereas the sign of the mean  $\text{EBF}_\tau'$  is of the correct sense to inject PV. The balance of these terms—particularly in realistic settings where models show that weakening of the mesoscale circulation by the CFB can lead to significant increases in baroclinic conversion of available potential energy by the submesoscale (Renault et al. 2018)—is not easily predicted. Given the interdependence of various dynamical properties of the submesoscale (including eddy buoyancy fluxes, TTW circulation, and the EBF) on common parameters such as the strength of the horizontal buoyancy gradients, future work should consider both direct and indirect pathways for air–sea interaction and coupling at the submesoscale.

## 5. Summary

In this manuscript a mechanism for the current feedback on the surface wind stress to affect submesoscale ocean fronts is identified through the Ekman buoyancy flux. Scaling arguments suggest that the CFB effect on the EBF can be significant in cases of strong surface currents, or cross-frontal winds, with examples from a numerical simulation showing approximately 25% changes in the local EBF due to the CFB. Importantly, this term acts primarily as a source of buoyancy to the mixed layer, or equivalently it acts to inject PV. This allows for even relatively modest changes to the EBF at individual fronts to contribute a significant change to the area-integral, reaching an approximately 50% reduction in the integrated EBF in the simulation shown here. Considering the CFB modification of the EBF may therefore be important to understanding the mixed layer buoyancy budget at both individual fronts in some cases, and when considering the integrated effects of the horizontal transport.

These changes can furthermore be directly related to changes in the frictional flux of PV, a key determinant of submesoscale mixed layer dynamics. The CFB is speculated to reduce both the frequency of occurrence of submesoscale symmetric instabilities, and the rate at which they extract and dissipate energy from the geostrophic flow field. Scaling arguments suggest that this mechanism may have energetic effects that are similar in magnitude to the effects of the CFB on the surface wind-work, and hence should be considered when looking at the energetic effects of the current feedback at submesoscale fronts. These effects may be particularly important in considering PV and buoyancy fluxes associated with submesoscale fronts embedded in more energetic mesoscale features, where the surface currents can be large. Examples of this occur frequently in mesoscale eddies, coastal fronts, and western boundary currents (Brannigan et al. 2017; D’Asaro et al. 2011; Zhang and Qiu 2018; Wenegrat et al. 2020).

The transition from the ocean mesoscale to the submesoscale is not just a change in length scale, but rather represents a change in dynamical regimes (Taylor and Thompson 2023). This indicates the possibility that other physical mechanisms

of air–sea interaction may be active at these scales, an example of which is the CFB modification of the EBF explored in this manuscript. However, disentangling the direct effects of the change of EBF versus other mechanisms emerging from the CFB on stress is challenging, even in the idealized numerical setup employed here. Further challenging is the potential importance of indirect effects (for instance the effect of the CFB on the TTW circulation and associated PV injection), which may have common parameter dependencies. Progress on the understanding of submesoscale air–sea interaction will be aided by consideration of the interplay of both direct and indirect effects of air–sea interaction processes, and how these might change in the dynamical transition from mesoscale to submesoscale.

**Acknowledgments.** The author thanks Jim Carton, Leah Johnson, Dimitris Menemenlis, Leif Thomas, and Ernesto Rodriguez for comments during preparation of this manuscript, and acknowledges the University of Maryland supercomputing resources (<http://hpcc.umd.edu>) made available for conducting the research reported in this paper. The input of two anonymous reviewers is also gratefully acknowledged. This work is a contribution to the S-MODE project (Farrar et al. 2020), an EVS-3 Investigation awarded under NASA Research Announcement NNH17ZDA001N-EVS3, and NASA Grant 80NSSC21K0554 awarded under NASA Research Announcement NNH20ZDA001N-PO to the University of Maryland, College Park.

**Data availability statement.** No observational data were used in this work. The model output is too large to be easily transferred but can be made available on request. Analysis code can be accessed at [https://github.com/wenegrat/cfb\\_on\\_ebf/releases/latest](https://github.com/wenegrat/cfb_on_ebf/releases/latest).

## REFERENCES

- Auclair, F., and Coauthors, 2022: Coastal and regional ocean community model, version 1.3. Zenodo, <https://doi.org/10.5281/ZENODO.7415055>.
- Bachman, S. D., B. Fox-Kemper, J. R. Taylor, and L. N. Thomas, 2017: Parameterization of frontal symmetric instabilities. I: Theory for resolved fronts. *Ocean Model.*, **109**, 72–95, <https://doi.org/10.1016/j.ocemod.2016.12.003>.
- Bishop, S. P., R. J. Small, and F. O. Bryan, 2020: The global sink of available potential energy by mesoscale air-sea interaction. *J. Adv. Model. Earth Syst.*, **12**, e2020MS002118, <https://doi.org/10.1029/2020MS002118>.
- Brannigan, L., D. P. Marshall, A. C. Naveira Garabato, A. J. G. Nurser, and J. Kaiser, 2017: Submesoscale instabilities in mesoscale eddies. *J. Phys. Oceanogr.*, **47**, 3061–3085, <https://doi.org/10.1175/JPO-D-16-0178.201>.
- Bye, J. A. T., 1985: Large-scale momentum exchange in the coupled atmosphere-ocean. *Coupled Ocean-Atmosphere Models*, Elsevier Oceanography Series, Vol. 40, Elsevier, 51–61, [https://doi.org/10.1016/S0422-9894\(08\)70702-5](https://doi.org/10.1016/S0422-9894(08)70702-5).
- Callies, J., and R. Ferrari, 2013: Interpreting energy and tracer spectra of upper-ocean turbulence in the submesoscale range (1–200 km). *J. Phys. Oceanogr.*, **43**, 2456–2474, <https://doi.org/10.1175/JPO-D-13-063.1>.

- , —, J. M. Klymak, and J. Gula, 2015: Seasonality in submesoscale turbulence. *Nat. Commun.*, **6**, 6862, <https://doi.org/10.1038/ncomms7862>.
- , G. Flierl, R. Ferrari, and B. Fox-Kemper, 2016: The role of mixed-layer instabilities in submesoscale turbulence. *J. Fluid Mech.*, **788**, 5–41, <https://doi.org/10.1017/jfm.2015.700>.
- Capet, X., J. C. McWilliams, M. J. Molemaker, and A. F. Shchepetkin, 2008: Mesoscale to submesoscale transition in the California Current System. Part I: Flow structure, eddy flux, and observational tests. *J. Phys. Oceanogr.*, **38**, 29–43, <https://doi.org/10.1175/2007JPO3671.1%201>.
- Chen, X., W. Dewar, E. Chassignet, M. Bourassa, S. Morey, and G. Gopalakrishnan, 2022: On the feedback between air-sea turbulent momentum flux and oceanic submesoscale processes. *J. Geophys. Res. Oceans*, **127**, e2022JC018767, <https://doi.org/10.1029/2022JC018767>.
- Chereskin, T. K., C. B. Rocha, S. T. Gille, D. Menemenlis, and M. Passaro, 2019: Characterizing the transition from balanced to unbalanced motions in the southern California Current. *J. Geophys. Res. Oceans*, **124**, 2088–2109, <https://doi.org/10.1029/2018JC014583>.
- Chor, T., J. O. Wenegrat, and J. Taylor, 2022: Insights into the mixing efficiency of submesoscale centrifugal-symmetric instabilities. *J. Phys. Oceanogr.*, **52**, 2273–2287, <https://doi.org/10.1175/JPO-D-21-0259.1>.
- D'Asaro, E., C. Lee, L. Rainville, R. Harcourt, and L. Thomas, 2011: Enhanced turbulence and energy dissipation at ocean fronts. *Science*, **332**, 318–322, <https://doi.org/10.1126/science.1201515>.
- Dewar, W. K., and G. R. Flierl, 1987: Some effects of the wind on rings. *J. Phys. Oceanogr.*, **17**, 1653–1667, [https://doi.org/10.1175/1520-0485\(1987\)017%3c1653:SEOTWO%3e2.0.CO;2](https://doi.org/10.1175/1520-0485(1987)017%3c1653:SEOTWO%3e2.0.CO;2).
- Duhaut, T. H. A., and D. N. Straub, 2006: Wind stress dependence on ocean surface velocity: Implications for mechanical energy input to ocean circulation. *J. Phys. Oceanogr.*, **36**, 202–211, <https://doi.org/10.1175/JPO2842.1>.
- Elipot, S., and J. Wenegrat, 2021: Vertical structure of near-surface currents: Importance, state of knowledge, and measurement challenges. *CLIVAR Variations*, Vol. 19, No. 1, U.S. CLIVAR Program, Washington, DC, 1–9, <https://doi.org/10.5065/ybca-0s03>.
- Farrar, J. T., and Coauthors, 2020: S-MODE: The sub-mesoscale ocean dynamics experiment. *IGARSS 2020–2020 IEEE Int. Geoscience and Remote Sensing Symp.*, Waikoloa, HI, Institute of Electrical and Electronics Engineers, 3533–3536, <https://doi.org/10.1109/IGARSS39084.2020.9323112>.
- Ferrari, R., and C. Wunsch, 2009: Ocean circulation kinetic energy: Reservoirs, sources, and sinks. *Annu. Rev. Fluid Mech.*, **41**, 253–282, <https://doi.org/10.1146/annurev.fluid.40.111406.102139>.
- González-Haro, C., and J. Isern-Fontanet, 2014: Global ocean current reconstruction from altimetric and microwave SST measurements. *J. Geophys. Res. Oceans*, **119**, 3378–3391, <https://doi.org/10.1002/2013JC009728>.
- , —, P. Tandeo, and R. Garello, 2020: Ocean surface currents reconstruction: Spectral characterization of the transfer function between SST and SSH. *J. Geophys. Res. Oceans*, **125**, e2019JC015958, <https://doi.org/10.1029/2019JC015958>.
- Isern-Fontanet, J., J. Ballabriga-Poy, A. Turiel, and E. García-Ladona, 2017: Remote sensing of ocean surface currents: A review of what is being observed and what is being assimilated. *Nonlinear Processes Geophys.*, **24**, 613–643, <https://doi.org/10.5194/npg-24-613-2017>.
- Johnson, L., C. M. Lee, E. A. D'Asaro, L. Thomas, and A. Shcherbina, 2020a: Restratification at a California Current upwelling front. Part I: Observations. *J. Phys. Oceanogr.*, **50**, 1455–1472, <https://doi.org/10.1175/JPO-D-19-0203.1>.
- , —, —, J. O. Wenegrat, and L. N. Thomas, 2020b: Restratification at a California Current upwelling front. Part II: Dynamics. *J. Phys. Oceanogr.*, **50**, 1473–1487, <https://doi.org/10.1175/JPO-D-19-0204.1>.
- Klein, P., B. L. Hua, G. Lapeyre, X. Capet, S. Le Gentil, and H. Sasaki, 2008: Upper ocean turbulence from high-resolution 3D simulations. *J. Phys. Oceanogr.*, **38**, 1748–1763, <https://doi.org/10.1175/2007JPO3773.1>.
- Lapeyre, G., 2017: Surface quasi-geostrophy. *Fluids*, **2**, 7, <https://doi.org/10.3390/fluids2010007>.
- Large, W. G., J. C. McWilliams, and S. C. Doney, 1994: Oceanic vertical mixing: A review and a model with a nonlocal boundary layer parameterization. *Rev. Geophys.*, **32**, 363–403, <https://doi.org/10.1029/94RG01872>.
- Luo, J.-J., S. Masson, E. Roeckner, G. Madec, and T. Yamagata, 2005: Reducing climatology bias in an ocean-atmosphere CGCM with improved coupling physics. *J. Climate*, **18**, 2344–2360, <https://doi.org/10.1175/JCLI3404.1>.
- Marshall, J., D. Jamous, and J. Nilsson, 2001: Entry, flux, and exit of potential vorticity in ocean circulation. *J. Phys. Oceanogr.*, **31**, 777–789, [https://doi.org/10.1175/1520-0485\(2001\)031<0777:EFAEOP>2.0.CO;2](https://doi.org/10.1175/1520-0485(2001)031<0777:EFAEOP>2.0.CO;2).
- McWilliams, J. C., 2017: Submesoscale surface fronts and filaments: Secondary circulation, buoyancy flux, and frontogenesis. *J. Fluid Mech.*, **823**, 391–432, <https://doi.org/10.1017/jfm.2017.294>.
- Miracca-Lage, M., C. González-Haro, D. C. Napolitano, J. Isern-Fontanet, and P. S. Polito, 2022: Can the Surface Quasi-Geostrophic (SQG) theory explain upper ocean dynamics in the South Atlantic? *J. Geophys. Res. Oceans*, **127**, e2021JC018001, <https://doi.org/10.1029/2021JC018001>.
- Naveira Garabato, A. C., X. Yu, J. Callies, R. Barkan, K. L. Polzin, E. E. Frajka-Williams, C. E. Buckingham, and S. M. Griffies, 2022: Kinetic energy transfers between mesoscale and submesoscale motions in the open ocean's upper layers. *J. Phys. Oceanogr.*, **52**, 75–97, <https://doi.org/10.1175/JPO-D-21-0099.1>.
- Pacanowski, R. C., 1987: Effect of equatorial currents on surface stress. *J. Phys. Oceanogr.*, **17**, 833–838, [https://doi.org/10.1175/1520-0485\(1987\)017<0833:EOECOS>2.0.CO;2](https://doi.org/10.1175/1520-0485(1987)017<0833:EOECOS>2.0.CO;2).
- Qiu, B., T. Nakano, S. Chen, and P. Klein, 2017: Submesoscale transition from geostrophic flows to internal waves in the northwestern Pacific upper ocean. *Nat. Commun.*, **8**, 14055, <https://doi.org/10.1038/ncomms14055>.
- Rai, S., M. Hecht, M. Maltrud, and H. Alarie, 2021: Scale of oceanic eddy killing by wind from global satellite observations. *Sci. Adv.*, **7**, eabf4920, <https://doi.org/10.1126/sciadv.abf4920>.
- Renault, L., M. J. Molemaker, J. Gula, S. Masson, and J. C. McWilliams, 2016a: Control and stabilization of the Gulf Stream by oceanic current interaction with the atmosphere. *J. Phys. Oceanogr.*, **46**, 3439–3453, <https://doi.org/10.1175/JPO-D-16-0115.1>.
- , —, J. C. McWilliams, A. F. Shchepetkin, F. Lemarié, D. Chelton, S. Illig, and A. Hall, 2016b: Modulation of wind work by oceanic current interaction with the atmosphere. *J. Phys. Oceanogr.*, **46**, 1685–1704, <https://doi.org/10.1175/JPO-D-15-0232.1>.
- , —, J. C. McWilliams, and S. Masson, 2017: Satellite observations of imprint of oceanic current on wind stress by air-sea

- coupling. *Sci. Rep.*, **7**, 17747, <https://doi.org/10.1038/s41598-017-17939-1>.
- , —, and J. Gula, 2018: Dampening of submesoscale currents by air-sea stress coupling in the Californian upwelling system. *Sci. Rep.*, **8**, 13388, <https://doi.org/10.1038/s41598-018-31602-3>.
- , P. Marchesiello, S. Masson, and J. C. McWilliams, 2019a: Remarkable control of western boundary currents by *eddy killing*, a mechanical air-sea coupling process. *Geophys. Res. Lett.*, **46**, 2743–2751, <https://doi.org/10.1029/2018GL081211>.
- , S. Masson, V. Oerder, S. Jullien, and F. Colas, 2019b: Disentangling the mesoscale ocean-atmosphere interactions. *J. Geophys. Res. Oceans*, **124**, 2164–2178, <https://doi.org/10.1029/2018JC014628>.
- Rooth, C., and L. Xie, 1992: Air-sea boundary layer dynamics in the presence of mesoscale surface currents. *J. Geophys. Res.*, **97**, 14 431–14 438, <https://doi.org/10.1029/92JC01296>.
- Schubert, R., J. Gula, R. J. Greatbatch, B. Baschek, and A. Biasottoch, 2020: The submesoscale kinetic energy cascade: Mesoscale absorption of submesoscale mixed layer eddies and frontal downscale fluxes. *J. Phys. Oceanogr.*, **50**, 2573–2589, <https://doi.org/10.1175/JPO-D-19-0311.1>.
- Seo, H., and Coauthors, 2023: Ocean mesoscale and frontal-scale ocean-atmosphere interactions and influence on large-scale climate: A review. *J. Climate*, **36**, 1981–2013, <https://doi.org/10.1175/JCLI-D-21-0982.1>.
- Shao, M., and Coauthors, 2019: The variability of winds and fluxes observed near submesoscale fronts. *J. Geophys. Res. Oceans*, **124**, 7756–7780, <https://doi.org/10.1029/2019JC015236>.
- Soares, S. M., S. T. Gille, T. K. Chereskin, E. Firing, J. Hummon, and C. B. Rocha, 2022: Transition from balanced to unbalanced motion in the eastern tropical Pacific. *J. Phys. Oceanogr.*, **52**, 1775–1795, <https://doi.org/10.1175/JPO-D-21-0139.1>.
- Soufflet, Y., P. Marchesiello, F. Lemarié, J. Jouanno, X. Capet, L. Debreu, and R. Benshila, 2016: On effective resolution in ocean models. *Ocean Modell.*, **98**, 36–50, <https://doi.org/10.1016/j.ocemod.2015.12.004>.
- Su, Z., J. Wang, P. Klein, A. F. Thompson, and D. Menemenlis, 2018: Ocean submesoscales as a key component of the global heat budget. *Nat. Commun.*, **9**, 775, <https://doi.org/10.1038/s41467-018-02983-w>.
- Sullivan, P. P., J. C. McWilliams, J. C. Weil, E. G. Patton, and H. J. S. Fernando, 2020: Marine boundary layers above heterogeneous SST: Across-front winds. *J. Atmos. Sci.*, **77**, 4251–4275, <https://doi.org/10.1175/JAS-D-20-0062.1>.
- Taylor, J. R., and R. Ferrari, 2010: Buoyancy and wind-driven convection at mixed layer density fronts. *J. Phys. Oceanogr.*, **40**, 1222–1242, <https://doi.org/10.1175/2010JPO4365.1>.
- , and A. F. Thompson, 2023: Submesoscale dynamics in the upper ocean. *Ann. Rev. Fluid Mech.*, **55**, 103–127, <https://doi.org/10.1146/annurev-fluid-031422-095147>.
- Thomas, L., and R. Ferrari, 2008: Friction, frontogenesis, and the stratification of the surface mixed layer. *J. Phys. Oceanogr.*, **38**, 2501–2518, <https://doi.org/10.1175/2008JPO3797.1>.
- Thomas, L. N., and C. M. Lee, 2005: Intensification of ocean fronts by down-front winds. *J. Phys. Oceanogr.*, **35**, 1086–1102, <https://doi.org/10.1175/JPO2737.1>.
- , J. R. Taylor, R. Ferrari, and T. M. Joyce, 2013: Symmetric instability in the Gulf Stream. *Deep-Sea Res. II*, **91**, 96–110, <https://doi.org/10.1016/j.dsr2.2013.02.025>.
- Wenegrat, J. O., and M. J. McPhaden, 2016: Wind, waves, and fronts: Frictional effects in a generalized Ekman model. *J. Phys. Oceanogr.*, **46**, 371–394, <https://doi.org/10.1175/JPO-D-15-0162.1>.
- , and R. S. Arthur, 2018: Response of the atmospheric boundary layer to submesoscale sea surface temperature fronts. *Geophys. Res. Lett.*, **45**, 13 505–13 512, <https://doi.org/10.1029/2018GL081034>.
- , L. N. Thomas, J. Gula, and J. C. McWilliams, 2018: Effects of the submesoscale on the potential vorticity budget of ocean mode waters. *J. Phys. Oceanogr.*, **48**, 2141–2165, <https://doi.org/10.1175/JPO-D-17-0219.1>.
- , —, M. A. Sundermeyer, J. R. Taylor, E. A. D’Asaro, J. M. Klymak, R. K. Shearman, and C. M. Lee, 2020: Enhanced mixing across the gyre boundary at the Gulf Stream front. *Proc. Natl. Acad. Sci. USA*, **117**, 17 607–17 614, <https://doi.org/10.1073/pnas.2005558117>.
- Xu, C., X. Zhai, and X.-D. Shang, 2016: Work done by atmospheric winds on mesoscale ocean eddies. *Geophys. Res. Lett.*, **43**, 12 174–12 180, <https://doi.org/10.1002/2016GL071275>.
- Zhang, Z., and B. Qiu, 2018: Evolution of submesoscale ageostrophic motions through the life cycle of oceanic mesoscale eddies. *Geophys. Res. Lett.*, **45**, 11 847–11 855, <https://doi.org/10.1029/2018GL080399>.